

## TOWARD FDS 6: COMPLEX GEOMETRY, EMBEDDED MESHES, AND QUALITY ASSESSMENT

Randall J. McDermott\*, Glenn P. Forney, Kevin McGrattan,  
and William E. Mell†

National Institute of Standards and Technology,  
Gaithersburg, Maryland, USA

\*Corresponding author email: randall.mcdermott@nist.gov

†National Institute of Standards and Technology,  
Boulder, Colorado, USA

**Key words:** Fire modeling, Large-eddy simulation, Immersed boundary method, Particle method, Nested grids, Quality assessment

**Abstract.** *The Fire Dynamics Simulator (FDS) and Smokeview (SMV) are computational and visualization tools specifically designed for large-eddy simulations (LES) of low-speed, thermally driven flows.<sup>1</sup> FDS Version 6 will offer improvements in the turbulence model (dynamic Smagorinsky<sup>2,3</sup>), the wall model (Werner Wengle<sup>4</sup>), and the scalar transport scheme (Superbee,<sup>5</sup> CHARM<sup>6</sup>). These features are already in the testing phase. In this work we discuss further developments related to complex geometry, embedded (or nested) mesh methods, and LES quality assessment. In FDS 6, we are developing two new approaches to handling complex geometry that take us beyond the limitations of the current stair-step method. For grid-resolved objects we are developing a complex geometry module with a second-order immersed boundary method capable of utilizing LES wall stress models.<sup>7</sup> For subgrid objects, such as electrical cables or vegetation in wildland fires, we are developing a particle-based approach, similar to a multi-phase droplet formulation, where the gas phase subgrid sources of mass, momentum, and energy are governed by empirical laws for pyrolysis, drag, and heat transfer, respectively.<sup>8</sup> Since LES quality is principally tied to grid resolution, in FDS 6 we introduce an embedded (or nested) mesh strategy which utilizes a staggered grid framework and a fast direct Poisson solver on each mesh block. We are also developing three strategies for quality assessment. The first is to compute local metrics of resolution such as the local fraction of resolved kinetic energy.<sup>9</sup> A second strategy is to use local wavelet-based error estimators.<sup>10</sup> Finally, with the latest release of Smokeview we have bundled a new executable called Smokediff. With this tool the user can compare results at different grid resolutions or with different model parameters and easily visualize the results.*

## 1 INTRODUCTION

The Fire Dynamics Simulator (FDS) and Smokeview (SMV) are computational and visualization tools specifically designed for large-eddy simulations (LES) of low-speed, thermally driven flows.<sup>1</sup> FDS Version 6 will offer improvements in the turbulence model (dynamic Smagorinsky<sup>2,3</sup>), the wall model (Werner Wengle<sup>4</sup>), and the scalar transport scheme (Superbee,<sup>5</sup> CHARM<sup>6</sup>). These features are already in the testing phase. In this work we discuss further developments related to complex geometry, embedded (or nested) mesh methods, and LES quality assessment.

In FDS 6, we are developing two new approaches to handling complex geometry that take us beyond the limitations of the current stair-step method. For grid-resolved objects we are developing a complex geometry module with a second-order immersed boundary method capable of utilizing LES wall stress models.<sup>7</sup> This is presented in Section 3.1. For subgrid objects, such as electrical cables or vegetation in wildland fires, we are developing a particle-based approach, similar to a multi-phase droplet formulation, where the gas phase subgrid sources of mass, momentum, and energy are governed by empirical laws for pyrolysis, drag, and heat transfer, respectively.<sup>8</sup> The particle method is described in Section 3.2.

Since LES quality is principally tied to grid resolution, in FDS 6 we introduce an embedded (or nested) mesh strategy which utilizes a staggered grid framework and a fast direct Poisson solver on each mesh block. The embedded mesh method is outlined in Section 4.

We are also developing strategies for LES quality assessment. The first is to compute local metrics of resolution such as the local fraction of resolved kinetic energy.<sup>9</sup> This is presented in Section 5.1. A second strategy, presented in Section 5.2, is to use a local wavelet-based error estimator.<sup>10</sup> Finally, as highlighted in Section 5.3, with the latest release of Smokeview we have bundled a new executable called *Smokediff*. With this tool the user can compare results at different grid resolutions or with different model parameters and easily visualize the results.

## 2 GOVERNING EQUATIONS

Details of the full FDS formulation may be found in the Technical Reference Guide.<sup>1</sup> It is useful, however, to briefly list the basic equations so that we may reference specific terms as we develop the methods later in the paper. FDS solves transport equations for density  $\rho$ , mass fraction of species  $Y_\alpha$ , and momentum  $u_i$  (see (1)-(3)). The equation of state and energy equations are combined with conservation of mass to provide a constraint on the velocity divergence (4).<sup>20</sup> Taking the divergence of the momentum equation provides an elliptic constraint on the pseudo-pressure  $\mathcal{H} \equiv p/\rho - K$ , where  $p$  is the fluctuating hydrodynamic pressure and  $K = \frac{1}{2}u_i u_i$  is the kinetic energy per unit mass. (Unless explicitly stated, Cartesian tensor suffix notation, e.g. contraction of repeated indices, applies throughout this paper.) Note that the momentum equation has been formulated

so that the Poisson equation for  $\mathcal{H}$  is separable. This permits the use of an extremely fast direct solution algorithm for (5).

$$\frac{\partial \rho}{\partial t} = -\frac{\partial \rho u_i}{\partial x_i} + \dot{m}_b''' \quad (1)$$

$$\frac{\partial \rho Y_\alpha}{\partial t} = -\frac{\partial F_{\alpha,i}}{\partial x_i} + \dot{m}_\alpha''' + \dot{m}_{\alpha,b}''' \quad (2)$$

$$\frac{\partial u_i}{\partial t} = -\left(F_{u,i} + \frac{\partial \mathcal{H}}{\partial x_i}\right) \quad (3)$$

$$\nabla \cdot \mathbf{u} = \frac{1}{\rho} \left( \dot{m}_b''' - \frac{D\rho}{Dt} \right) \quad (4)$$

$$\frac{\partial^2 \mathcal{H}}{\partial x_i \partial x_i} = -\left( \frac{\partial F_{u,i}}{\partial x_i} + \frac{\partial (\nabla \cdot \mathbf{u})}{\partial t} \right) \quad (5)$$

### 3 COMPLEX GEOMETRY

In this section we address complex geometry by approaching the problem from two different directions. First, we discuss a method to handle complex shapes that are resolved by the grid. Then we discuss a way to handle objects which are unresolved by the fluid mesh, but still significantly influence the flow through sources or sinks of mass, momentum, and energy.

#### 3.1 Implementation of LES Wall Models in Direct Forcing IBM

In an immersed boundary method (IBM) the influence of geometry enters the formulation through a body force term in the momentum equation. By augmenting the RHS of the momentum equation (and hence the source term in the Poisson equation) the elliptic solve is greatly simplified and we may still use fast solvers on block structured domains. To simplify matters further, Fadlun et al.<sup>11</sup> introduced the notion of *direct forcing* IBM in which the body force is formulated to simply cancel out most of the RHS and directly force a given velocity component to a desired value. Thus, for a simple explicit time update, the body force term in the momentum equation becomes

$$F_{u,i}^{ibm} = -\left[ \frac{u_i^{ibm} - u_i^n}{\delta t} + \frac{\delta \mathcal{H}^n}{\delta x_i} \right] \quad (6)$$

When this force is used in the momentum equation (3) the projection scheme drives the velocity  $u_i^{n+1}$  toward  $u_i^{ibm}$ . For a purely explicit scheme, in most cases the error is remarkably small. For an implicit scheme, the error may be driven to a desired tolerance by Picard iteration.

The direct forcing approach is attractive because it reduces the problem to determining the value of  $u_i^{ibm}$ . For example, on a Cartesian staggered grid, the impermeability

condition is obtained by simply setting  $u_i^{ibm} = 0$ . This has been and remains the standard mode of operation in FDS. Fadlun et al. showed that this results in zeroth order errors for representing curved surfaces. Fadlun et al. go on to develop a second-order interpolation method for direct numerical simulation (DNS). In this work we address the problem of implementing an LES wall model.

The idea presented here is really just an exercise in computational geometry. The problem we are faced with is that LES wall models supply a formula for the wall stress based on the streamwise velocity and the normal distance from the wall. So, to use this model we need to first translate the available data from our original grid system to a streamwise coordinate system. Once this is done, the wall model is rather simple to implement (minus a trick to overcome the potential time step limitation). We can then transfer the information from the wall model back to our original coordinate system.

**Formulation** Much of the background needed for this section can be found in the Appendix A of Pope.<sup>12</sup> Let us denote the orthonormal basis vectors for our grid system by  $\mathbf{e}_i$  where  $i = \{1, 2, 3\}$ . The basis vectors for the streamwise coordinate system are  $\bar{\mathbf{e}}_i$ ,  $i = \{1, 2, 3\}$ . Figure 1 illustrates the relationship between the two systems. The basis  $\bar{\mathbf{e}}_2$  in this 2D case is the surface unit normal vector which emanates from  $\mathbf{x}_{surf}$  and is directed toward the point  $\mathbf{x}_{velo}$ , the storage location for the staggered velocity component. The point marked by the cross is labeled  $\mathbf{x}_{int}$  and is twice the distance along the normal line from  $\mathbf{x}_{surf}$ .

The elements of the directional cosine matrix are found from the dot product of the basis vectors:

$$a_{ij} = \mathbf{e}_i \cdot \bar{\mathbf{e}}_j \quad (7)$$

This matrix is the key to simple translation from one coordinate system to another. Once the directional cosines are obtained we may rotate the velocity vector, the velocity gradient tensor, and the stress tensor into the streamwise system via ( $g_{ij}$  represents a general tensor element)

$$\bar{u}_k = a_{ik} u_i \quad (8)$$

$$\bar{g}_{kl} = a_{ik} a_{jl} g_{ij} \quad (9)$$

Once the system has been rotated we make an explicit update of the boundary layer equations. Here, superscript  $k$  denotes a time index, subscript  $w$  denotes a wall value,  $\delta n$  indicates a value stored at  $\mathbf{x}_{velo}$ , and  $2\delta n$  indicates a value stored at  $\mathbf{x}_{int}$  in the grid system. The wall-normal component is updated by

$$\bar{v}^{k+1} = \bar{v}_w + \delta n \left( \nabla \cdot \mathbf{u}^{k+1} - \frac{1}{2} \frac{\partial \bar{u}}{\partial s} \Big|_{2\delta n}^k \right) \quad (10)$$

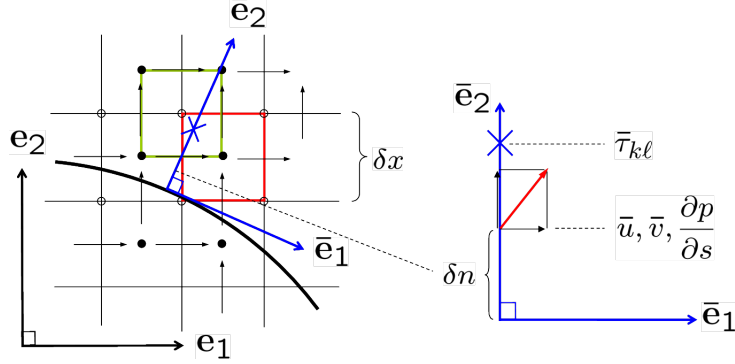


Figure 1: Grid and streamwise coordinate systems for the immersed boundary method.

and the RHS of the streamwise component is discretized by

$$\frac{d\bar{u}}{dt} = - \left[ \bar{u} \frac{1}{2} \frac{\partial \bar{u}}{\partial s} \Big|_{2\delta n}^k + \bar{v}^{k+1} \frac{1}{2} \left( \frac{\partial \bar{u}}{\partial n} \Big|_{2\delta n}^k + \frac{\partial \bar{u}}{\partial n} \Big|_w \right) + \frac{1}{\rho} \left( \frac{\partial p}{\partial s} \Big|_{\delta n}^k + \frac{\bar{\tau}_{sn}|_{2\delta n}^k - \bar{\tau}_{sn}|_w}{2\delta n} \right) \right] \quad (11)$$

The key point to appreciate is that  $\bar{\tau}_{sn}|_w$  may now easily be evaluated from a wall model like Werner and Wengle.<sup>4</sup>

Because  $\delta n$  may become arbitrarily small, a stable explicit time step might also become too small for practical purposes. To avoid this issue, we rewrite (11) as the following ODE

$$\frac{d\bar{u}}{dt} = a\bar{u} + b \quad (12)$$

which has the stable solution

$$\bar{u}(t) = \frac{(a\bar{u}_0 + b)e^{at} - b}{a} \quad (13)$$

Finally, we transform the velocity vector back to the grid system for use in the direct forcing IBM

$$u_i^{ibm} = a_{ik}\bar{u}_k \quad (14)$$

## Summary of the Wall Model IBM Method

1. For a given velocity component, determine whether or not the staggered storage location is inside (or exactly on) the geometry, purely in the fluid phase, or (more interestingly) within the “surface layer” and thus needs special treatment.
2. For velocity cells within the surface layer, based on the current position and orientation of the geometry, find the line that is normal to the surface and passes through the staggered velocity component location.

3. Determine the distance  $\delta n$  from  $\mathbf{x}_{velo}$  to  $\mathbf{x}_{surf}$  and define the point  $\mathbf{x}_{int}$  as the point on the normal line  $2\delta n$  from the surface. This point is marked as the blue  $\times$  in Figure 1.
4. Interpolate the additional velocity components, velocity divergence (determined from (4)), and the density to  $\mathbf{x}_{velo}$ . Also, interpolate the turbulent viscosity and the nine components of the velocity gradient to  $\mathbf{x}_{int}$ .
5. Compute the pressure gradient at  $\mathbf{x}_{velo}$  and, from the interpolated velocity gradient, compute the stress tensor (including turbulent stress) at  $\mathbf{x}_{int}$ .
6. Determine the “streamwise” coordinate system: Find the vector in the tangent plane of the surface that is orthogonal to the relative velocity between the fluid and the surface,  $\mathbf{t} = \hat{\mathbf{n}} \times (\mathbf{u} - \mathbf{u}_w)$ , and normalize,  $\hat{\mathbf{t}} = \mathbf{t}/\|\mathbf{t}\|$ . Define the streamwise coordinate by  $\hat{\mathbf{s}} = \hat{\mathbf{t}} \times \hat{\mathbf{n}}$ . The new orthonormal basis is now  $\{\bar{\mathbf{e}}_1, \bar{\mathbf{e}}_2, \bar{\mathbf{e}}_3\} = \{\hat{\mathbf{s}}, \hat{\mathbf{t}}, \hat{\mathbf{n}}\}$ . Note that because of this choice the relative velocity component in the  $\hat{\mathbf{t}}$  direction will always be zero.
7. Transform the pressure gradient, the velocity gradient, and the stress tensor into the streamwise coordinate system via (8) and (9).
8. Update the wall normal velocity component and the streamwise relative velocity via (10) and (11), in that order.
9. Transform back to the grid system via (14) and use the resulting velocity component in the direct forcing IBM.

**Results** We test the approach on a simple geometric object, a sphere, which is “complex geometry” for a Cartesian grid. Figure 2 shows results for two cases. On the left we have a 2D calculation of a rotating disk in an enclosed cavity. The disk rotates at  $2\pi$  radians per second and the no slip condition applies at all surfaces. The arrows indicate velocity vectors colored by velocity magnitude. The Reynolds number for this case is approximately 4. On the right we show a snapshot from a simulation of a 90 mile per hour (mph) fastball rotating at 20 revolutions per second.<sup>17</sup> The motion of the geometry is prescribed, but the geometry does influence the fluid (a one-way coupling). The Reynolds number for this flow is approximately  $2 \times 10^5$ . In the future, two-way fluid-structure interaction is planned.

### 3.2 Using Lagrangian Particles to Model Complex Subgrid Objects

There are many real objects that participate in a fire that cannot be modeled easily as solid obstructions that conform to the rectilinear mesh. For example, electrical cables, dry brush, tree branches and so on, are potential fuels that cannot be well-represented as

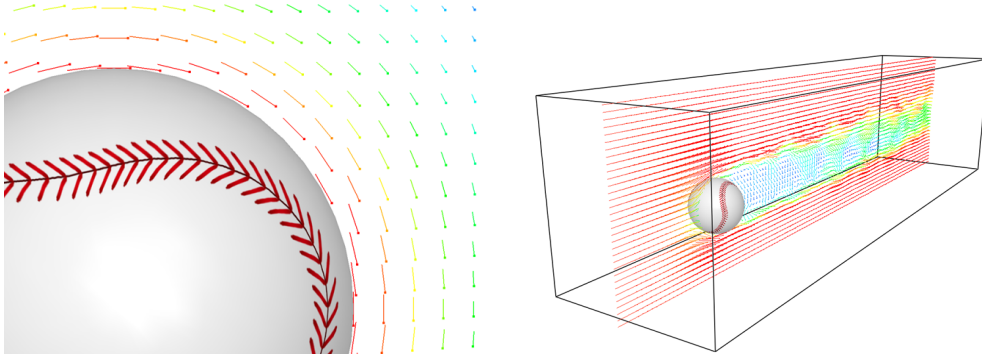


Figure 2: (Left) 2D calculation of a stationary rotating disk,  $Re = 4$ . (Right) Snapshot of a translating and rotating sphere (90 mph fastball),  $Re \approx 2 \times 10^5$ .

solid cubes, not only because the geometry is wrong, but also because the solid restricts the movement of hot gases through the complex collection of objects. As a potential remedy for the problem, these objects can be modeled as discrete particles that are either spheres, cylinders or small sheets. Each particle can be assigned a set of properties in much the same way as is done for solid obstructions that conform to the numerical grid. The particle is assumed to be thermally-thick, but for simplicity the heat conduction within the particle is assumed to be one-dimensional in either a cylindrical, spherical or cartesian coordinate system. The LES filter formalism for this approach is discussed in Mell et al.<sup>8</sup> The basic function of the method is to supply bulk mass, momentum, and energy source terms in (1)-(4).

Figure 3 shows a recent experiment conducted at NIST on behalf of the U.S. Nuclear Regulatory Commission. The purpose of the experiment was to measure the heat release rate of a tray of burning electrical cables when exposed to a heat flux from the radiant panels overhead. The simulation uses Lagrangian particles to represent 10 cm segments of the cables. The cables are assumed to be cylindrical objects with an outer layer of plastic (the cable “jacket”) and an inner layer that consists of a mixture of copper and plastic (the conductors and insulation material). The random distribution of the cable segments is intended to mimic the way cables are typically run through ladder-back trays. Bench-scale experiments are underway to characterize the thermo-physical properties of the plastic materials. The goal of the modeling effort is to capture as much of the detail of the cable under the assumption of one-dimensional heat conduction in the radial direction over a length that is roughly equal to the size of a single grid cell.

## 4 EMBEDDED MESHES

Cartesian grids are notoriously poor at optimizing mesh density, especially for LES where locally cubic cells are required to resolve three-dimensional turbulent motion. As reviewed in Schneider and Vasilyev,<sup>10</sup> the future potentially holds very elegant and sophis-

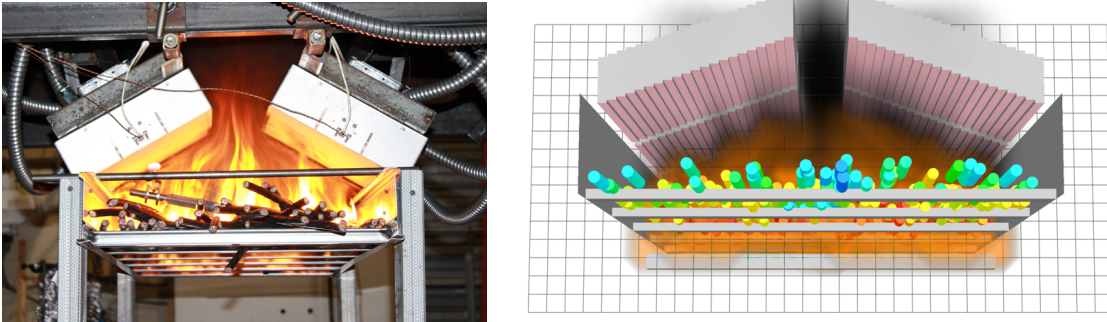


Figure 3: Cable fire experiment performed for the U.S. Nuclear Regulatory Commission. (Left) Photo from experiment where radiant panels heat electrical cables to the point of ignition. (Right) FDS calculation using the subgrid particle method. Color represents particle temperature.

ticated ways of addressing this problem. Currently, FDS is capable of what is sometimes called ‘one-way’ nesting or ‘down-scaling’ in the atmospheric community.<sup>18</sup> That is, one mesh may be nested within another and the fine mesh will use the background mesh for its boundary conditions. However, no information is passed from the fine mesh back to the coarse mesh. As we move forward in fire modeling, there are many applications where a dynamic two-way coupling between the coarse and fine mesh would be useful. The fact that wild fires can actually alter weather patterns highlights the problem.

An example of dynamic two-way coupling between meshes is illustrated in Figure 4 where we are simulating the Sandia 1 m helium plume, a case that will be studied further in the next section on quality assessment. To the left side of the figure we see the fine mesh (red) embedded within the coarse mesh (black). The outer domain is  $2 \times 2 \times 4 \text{ m}^3$ . The coarse mesh spacing is roughly 6 cm and the fine mesh spacing is 1.5 cm (4:1 ratio). The green dots represent measurement locations which will be used for data comparisons later in this paper. On the right side of the figure we show an instantaneous contour plot of helium mass fraction. Note the difference in resolution within and outside the boundary of the fine mesh.

The methodology employed in FDS is based largely on the framework concepts developed at Lawrence Livermore National Laboratories<sup>19</sup> and Lawrence Berkeley National Laboratory.<sup>20</sup> The basic idea is to consider a mesh hierarchy: a coarse mesh  $M_1$  and a fine mesh  $M_2$ . The coarse mesh provides boundary conditions for the fine mesh and the fine mesh provides fluxes and source terms to the coarse mesh through averaging operators. The staggered grid arrangement actually simplifies these operators substantially over other AMR schemes.

Below we provide a brief description of a single forward Euler step in the algorithm (in the actual code the scheme is a second-order predictor/corrector). The key steps, which differ from the normal FDS scheme are Steps 2, 3, 6, 8, and 9. At present, strong momentum source terms which are “invisible” to the coarse mesh are not properly handled.



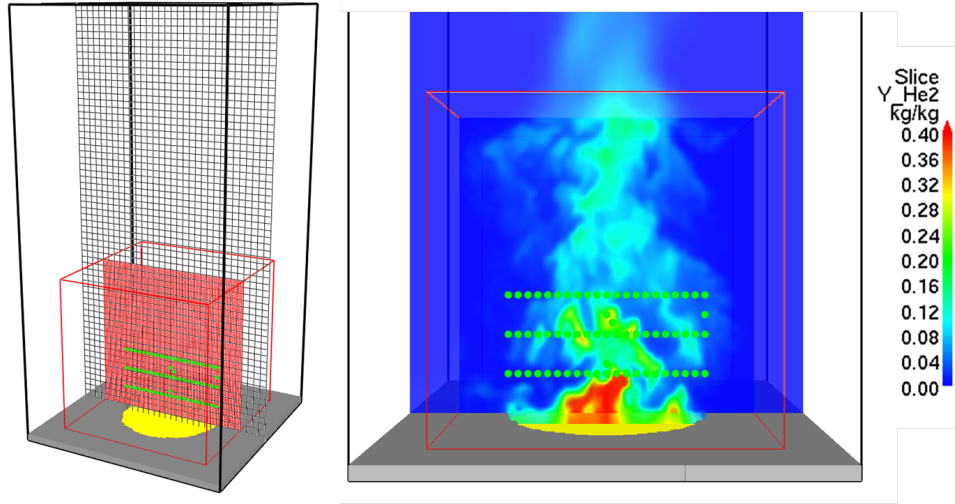


Figure 4: (Left) Helium plume embedded mesh: 1 m plume diameter, 4:1 grid ratio. (Right) Instantaneous contours of helium mass fraction.

This is a topic under current development.

### Summary of the Embedded Mesh Method (Forward Euler Version)

1. Given a consistent velocity and scalar field between  $M_1$  and  $M_2$ , compute scalar fluxes on all faces for both meshes.
2. For all coincident faces, including the boundary of  $M_2$ , replace the  $M_1$  flux with the average of the  $M_2$  fluxes.
3. Compute the RHS of the momentum equation and advance the scalar transport equation for both meshes (reaction source terms for  $M_1$  are obtained from a restriction of  $M_2$ ).
4. Update  $M_2$  ghost cell values from  $M_1$ .
5. Compute the velocity divergence on each mesh.
6. Restrict the divergence from  $M_2$  to  $M_1$ .
7. Build the RHS of the Poisson equation, solve for the pressure, and correct the velocity on each mesh.
8. Apply the  $M_1$  (coarse mesh) velocity to the boundary of  $M_2$ .
9. Project the velocity on  $M_2$  to satisfy the divergence constraint.
10. Apply tangential boundary conditions to each mesh. *End*

## 5 QUALITY ASSESSMENT

As stated in the introduction, the subject of LES quality assessment goes beyond the issues of verification and validation. One should envision working with a code which has been subjected to and passed all manner of V&V protocols and then being tasked with answering the question of whether or not a given LES result (or set of results) satisfactorily answers the engineering or design question at hand. And this is to be done in the absence of experimental data. Assuming the LES code obeys the principle of LES to DNS convergence (and this is by no means guaranteed), the quality of a particular result is most directly tied to grid resolution. In the sections to follow we examine ways to measure mesh resolution quality.

In the fire modeling literature, the workhorse metric for assessing grid resolution is the quantity  $D^*/\delta x$  (note that here we consider implicitly filtered, energy-conserving schemes; thus the mesh spacing is equal to the LES filter width), where  $D^*$  is the characteristic length scale of the fire. It is a dimensional quantity obtained from the total heat release rate  $\dot{Q}$  and ambient density, specific heat, and temperature,

$$D^* = \left( \frac{\dot{Q}}{\rho_\infty c_p T_\infty \sqrt{g}} \right)^{\frac{2}{5}} \quad (15)$$

As a rough rule of thumb,  $D^*/\delta x \approx 10$  has historically been considered adequate grid resolution.

This rule of thumb is attractive for simple pool fire or well-defined compartment fire scenarios, but in general is fraught with problems. Not the least of which is that it is based more on what is (or was) computationally affordable than what is demanded by the physics of the problem. It was developed within codes that were not convergent and which were basically tuned to make that particular resolution work. As we move forward toward problems such as fire spread we need better ways to assess the quality of our results.

Below we describe output quantities and tools to aid FDS users in quality assessment. Two output quantities are suggested for measuring errors in the velocity and scalar fields. Respectively, these measures are: (1) a model for the fraction of unresolved kinetic energy<sup>9</sup> (similar to what is often called the ‘Pope criterion’) and (2) a wavelet-based error measure inspired by the works of Schneider and Vasilyev,<sup>10</sup> though our approach is quite simple at the present time.

While the Pope criterion has a known cutoff for the canonical case of homogeneous isotropic turbulence (it can be shown that resolving 80% of the kinetic energy puts the grid Nyquist limit into the inertial subrange), in general we do not know *a priori* what cutoff should be used. Indeed, some would rightly argue that this completely depends on what question is being addressed in running the model.<sup>16</sup> Here we take the practical attitude that we want our model results to fall within the uncertainty bounds of the (perhaps hypothetical) experimental data. However, as stated above, the quality measures

are ultimately only useful if they function without the need for data. To achieve this state of confidence, the measures must be vetted for a broad range of applications. The vetting process needs to consider three specific grid resolutions: two showing satisfactory and converging results, and a third coarser calculation showing unsatisfactory results. We denote these resolutions as under-resolved, resolved, and over-resolved. Ideally, the under-resolved case is within a factor of 2 of the resolved case. The point of the exercise is to delineate satisfactory from unsatisfactory values of the metric. The over-resolved case is needed to ensure convergence (i.e. that the resolved result is not fortuitous).

To illustrate the process, below we examine mean radial profiles of vertical velocity and scalar concentration for the Sandia 1 m helium plume experiment.<sup>14,15</sup> Details of the experiment are provided in the references and FDS input files are available in our code repository.<sup>1</sup> Nominally, 0.06 kg/m<sup>2</sup>/s of a helium/acetone mixture ( $W = 5.45$ ) issues from a 1 m diameter source into a quiescent environment. The computational domain is set at  $2 \times 2 \times 4$  m<sup>3</sup> in the  $x, y, z$  dimensions ( $z$  is the vertical dimension). The calculations are run in parallel with 16 processors with a simple domain decomposition of 16 1 m<sup>3</sup> blocks. Three grid resolutions are run at nominally  $\{1.5, 3, 6\}$  cm resolution ( $64^3, 32^3$ , and  $16^3$  cells for each 1 m<sup>3</sup> block). The results for the mean radial profiles of vertical velocity and helium mass fraction at 3 downstream locations corresponding to  $z/D = \{0.2, 0.4, 0.6\}$  are shown in Figure 5. The results are rather insensitive to the grid resolution, except for the result for vertical velocity at  $z/D = 0.2$  (lower left). Though this may arguably be related to the uncertainty of the inflow boundary condition (constant and uniform inlet conditions are specified), we will nevertheless examine the proposed quality metrics to see what (if any) patterns emerge.

### 5.1 Measure of Turbulence Resolution

In FDS, the user may output a scalar quantity which we refer to as the ‘measure of turbulence resolution’, defined locally as

$$\text{MTR}(\mathbf{x}, t) = \frac{k_{sgs}}{k_{res} + k_{sgs}} \quad (16)$$

where

$$k_{res} = \frac{1}{2} \bar{u}_i \bar{u}_i \quad (17)$$

$$k_{sgs} = \frac{1}{2} (\bar{u}_i - \hat{u}_i)(\bar{u}_i - \hat{u}_i) \quad (18)$$

Here,  $\bar{u}_i$  is the resolved LES velocity and  $\hat{u}_i$  is test filtered at a scale  $2\Delta$ . The basic idea is to provide the user with an approximation to the Pope criterion,<sup>9</sup>  $M$ , which is easily accessible in Smokeview (the FDS visualization tool). In Smokeview, the user may readily time average MTR in a specified plane. The time average of MTR is a reasonable estimate of  $M$ . The measure falls within the range  $[0,1]$ , with 0 indicating a perfect resolution and

1 indicating poor resolution. The concept is illustrated in Figure 6. Notice that on the left the difference between the grid signal and the test signal is very small. On the right, the grid signal is highly turbulent and the corresponding test signal is smooth. We infer then that the flow is under-resolved.

For the canonical case of isotropic turbulence Pope actually defines LES such that  $M < 0.2$ . That is, LES requires resolution of 80% of the kinetic energy in the flow field (because this puts the grid Nyquist limit within the inertial subrange). The question remains as to whether this critical value is sufficient or necessary for a given engineering problem. Figure 7 shows time averages of MTR for the three resolutions used for this study. It can be seen that the under-resolved case ( $\delta x = 6$  cm, far left) shows many excursions above 0.4, whereas for the resolved case (center) most of the shear layer between the plume and the ambient surroundings sees an average MTR of roughly 0.2, though there are small regions with significant deviations. The over-resolved case (right) maintains average values of MTR below 0.2. It seems, therefore, that the canonical example provides good insight to buoyant plume problems. And perhaps this is to be expected since plumes are similar to decaying isotropic turbulence in a Lagrangian frame.

## 5.2 Wavelet Error Measure

We begin by providing background on the simple Haar wavelet. For a thorough and more sophisticated review of wavelet methods, the reader is referred to Schneider and Vasilyev.<sup>10</sup>

Suppose the scalar function  $f(r)$  is sampled at discrete points  $r_j$  giving values  $s_j$ . Defining the *unit step function* over the interval  $[r_1, r_2]$  by

$$\varphi_{[r_1, r_2]} = \begin{cases} 1 & \text{if } r_1 \leq r < r_2 \\ 0 & \text{otherwise} \end{cases} \quad (19)$$

the simplest possible reconstruction of the signal is the step function approximation

$$f(r) \approx \sum_j s_j \varphi_{[r_j, r_j+h]}(r) \quad (20)$$

By “viewing” the signal at a coarser resolution, say  $2h$ , an identical reconstruction of the function  $f$  over the interval  $[r_j, r_j + 2h]$  may be obtained from

$$f_{[r_j, r_j+2h]}(r) = \underbrace{\frac{s_j + s_{j+1}}{2}}_a \varphi_{[r_j, r_j+2h]}(r) + \underbrace{\frac{s_j - s_{j+1}}{2}}_c \psi_{[r_j, r_j+2h]}(r) \quad (21)$$

where  $a$  is the *average* coefficient and  $c$  is the *wavelet* coefficient. The Haar *mother wavelet* (Figure 8) is given by

$$\psi_{[r_1, r_2]}(r) = \begin{cases} 1 & \text{if } r_1 \leq r < \frac{1}{2}(r_1 + r_2) \\ -1 & \text{if } \frac{1}{2}(r_1 + r_2) \leq r < r_2 \end{cases} \quad (22)$$

The decomposition of the signal shown in (21) may be repeated at ever coarser resolutions. The result is a *wavelet transform*. The procedure is entirely analogous to the Fourier transform, but with compact support. If we look at a 1D signal with  $2^m$  points, the repeated application of (21) results in an  $m \times m$  matrix of averages  $\mathbf{a}$  with components  $a_{ij}$  and an  $m \times m$  wavelet coefficient matrix  $\mathbf{c}$  with components  $c_{ij}$ . Each row  $i$  of  $\mathbf{a}$  may be reconstructed from the  $i + 1$  row of  $\mathbf{a}$  and  $\mathbf{c}$ . Because of this and because small values of the wavelet coefficient matrix may be discarded, dramatic compression of the signal may be obtained.

We are interested in using a wavelet analysis to say something about the local level of error in grid resolution. Very simply, we ask what can be discerned from a sample of 4 data points along a line. Roughly speaking we might expect to see one of the four scenarios depicted in Figure 9. Within each plot window we also show the results of a Haar wavelet transform for that signal. Looking first at the two top plots, on the left we have a step function and on the right we have a straight line. Intuitively, we expect large error for the step function and small error for the line. The following error measure achieves this goal:

$$\text{WEM}(\mathbf{x}, t) = \max_{x,y,z} \left( \frac{|\sum_j c_{1j}| - |c_{21}|}{|a_{21}|} \right) \quad (23)$$

Note that we have arbitrarily scaled the measure so that a step function leads to WEM of unity. In practice the transform is performed in all coordinate directions and the max value is reported. The scalar value may be output to Smokeview at the desired time interval. Looking now at the two plots on the bottom of Figure 9, the signal on the left, which may indicate spurious oscillations or unresolved turbulent motion, leads to  $\text{WEM} = 2$ . Our measure therefore views this situation as the worst case in a sense. The signal to the lower right is indicative of an extremum, which actually is easily resolved by most centered spatial schemes and results again in  $\text{WEM} = 0$ .

Time averages of WEM for the helium case at three resolutions are shown in Figure 10. The under-resolved case (left) sees a large region near the base of the plume where  $\text{WEM} > 1$ . The average value along the shear layer is near 0.75. For the resolved case (center) we still see small excursions above unity near the base, but the majority of the shear layer remains near 0.5. Though, within the downstream distances we are examining ( $z/D \leq 0.6$ ) we see WEM near 0.75 in places. Even the over-resolved case sees excursions above unity near the lip of the plume. These are areas of the flow where given perfect economy of grid points (nonuniform grids) we would choose to concentrate our resolution. However, it is evident *a posteriori* that small excursions of WEM near unity may be permissible for statistically stationary flows such as the helium plume. From these images and comparison with the data, it seems that an optimal value for WEM is near 0.5.

### 5.3 Smokediff

Smokediff is a new package bundled with the latest release of Smokeview, the FDS visualization tool. Further details are provided in the Smokeview User’s Guide.<sup>1</sup> With Smokediff the user may easily compare the outputs of two different FDS runs using different model parameters or different mesh resolutions, for example. In the case of comparing runs with different resolutions, the output from Smokediff may be viewed as a signed error, taking the finer mesh as the true value. Though the chaotic nature of the flows often makes the instantaneous errors look large, the time average of the differences can be insightful.

## 6 CONCLUSIONS

In this paper we have presented a novel approach to implementing wall models in a direct forcing immersed boundary method. We have demonstrated the accuracy and robustness of the approach spanning five orders of magnitude in Reynolds number. The ODE solution for the streamwise velocity component gracefully handles the small cutcell problem. At the opposite end of the mesh resolution spectrum, we have demonstrated the feasibility of applying convective and radiant heat transfer models to subgrid particle methods for fire dynamics. The method has applicability in both industrial and wild fire scenarios.

A method for two-way coupling between coarse and fine meshes is outlined and demonstrated. For the problem considered in this work, the 1 m helium plume, a node reduction of more than a factor of four is realized for the embedded mesh case. The method greatly simplifies the problem of multi-resolution 3D mesh generation in FDS. Several practical issues remain to be solved before the embedded mesh method is ready for general use. These issues include the proper treatment of grossly under-resolved momentum sources (e.g., jets) which are invisible to the coarsest background mesh.

Lastly, we have developed and demonstrated two methods for assessing LES quality. One method provides a measure of turbulence resolutions (MTR) based on the idea of Pope’s criterion.<sup>9</sup> By comparing with experimental data at three different grid resolutions, we conclude that the theoretical value of  $\langle \text{MTR} \rangle = 0.2$  (brackets indicate a time average) provides a good target for assuring LES quality for buoyant plumes. Additionally, we present a new idea for estimating errors in the scalar field based on a simple local Haar wavelet analysis. The method looks at a sample of four points in a given direction and from the wavelet coefficients infers an error level. Based on the chosen scaling for the WEM metric, we find that a value of  $\langle \text{WEM} \rangle = 0.5$  provides a good target error level for optimal mesh resolution in stationary buoyant plumes.

## ACKNOWLEDGEMENTS

The authors would like to thank the U.S. Nuclear Regulatory Commission and the U.S. Forest Service for their financial support.

## REFERENCES

- [1] <http://fire.nist.gov/fds>
- [2] M. Germano, U. Piomelli, P. Moin and W. Cabot, A dynamic subgrid-scale eddy viscosity model, *Phys. Fluids A*, **3**(7), 1760-1765 (1991).
- [3] P. Moin, K. Squires, W. Cabot and S. Lee, A dynamic subgrid-scale model for compressible turbulence and scalar transport, *Phys. Fluids A*, **3**(11), 2746-2757 (1991).
- [4] H. Werner and H. Wengle, Large-eddy simulation of turbulent flow over and around a cube in a plate channel, In *8th Symposium on Turbulent Shear Flows*, 155-168 (1991).
- [5] P. L. Roe, Characteristics-based schemes for the Euler equations, *Ann. Rev. Fluid Mech.*, **18**, 337 (1986).
- [6] G. Zhou, Numerical simulations of physical discontinuities in single and multi-fluid flows for arbitrary Mach numbers, PhD Thesis, Chalmers University of Technology, Goteborg, Sweden (1995).
- [7] R. McDermott, G. Forney, C. Cruz and K. McGrattan, A second-order immersed boundary method with near-wall physics, In *The 62nd Annual Meeting of the American Physical Society's Division of Fluid Dynamics*, Minneapolis, Minnesota (2009).
- [8] W. Mell, A. Maranghides, R. McDermott and S. Manzello, Numerical simulation and experiments of burning Douglas fir trees, *Combust. Flame*, **156**, 2023-2041 (2009).
- [9] S. B. Pope, Ten questions concerning the large-eddy simulation of turbulent flows, *New J. Phys.*, **6**, 1-24 (2004).
- [10] K. Schneider and O. Vasilyev, Wavelet Methods in Computational Fluid Dynamics, *Annu. Rev. Fluid Mech.*, **42**, 473-503 (2010).
- [11] E. A. Fadlun, R. Verzicco, P. Orlandi and J. Mohd-Yusof, Combined Immersed-Boundary Finite-Difference Methods for Three-Dimensional Complex Flow Simulations, *J. Comp. Phys.*, **161**, 35-60 (2000).
- [12] Stephen B. Pope, Turbulent Flows, *Cambridge* (2000).
- [13] Yves Nievergelt, Wavelets Made Easy, *Birkhäuser* (2001).
- [14] P. E. DesJardin, T. J. O'Hern, and S. R. Tieszen, Large eddy simulation and experimental measurements of the near-field of a large turbulent helium plume, *Phys. Fluids*, **16**, 1866-1883 (2004).

- [15] T. J. O'Hern, E. J. Weckman, A. L. Gerhart, S. R. Tieszen, and R. W. Schefer, Experimental study of a turbulent buoyant helium plume, *J. Fluid Mech.*, **544**, 143-171 (2005).
- [16] W. L. Oberkampf and M. F. Barone, Measures of agreement between computation and experiment: Validation metrics, *J. Comp. Phys.*, **217**, 5-36 (2006).
- [17] A. T. Bahill, D. G. Baldwin, and J. S. Ramberg, Effects of altitude and atmospheric conditions on the flight of a baseball, *Int. J. Sports Sci. Eng.*, **3** 109-128 (2009).
- [18] Eugenia Kalnay, Atmospheric Modeling, Data Assimilation, and Predictability, *Cambridge* (2003).
- [19] <http://www.llnl.gov/CASC/SAMRAI>
- [20] J. B. Bell, AMR for low Mach number reacting flow, *Paper LBNL-54351* (2004).



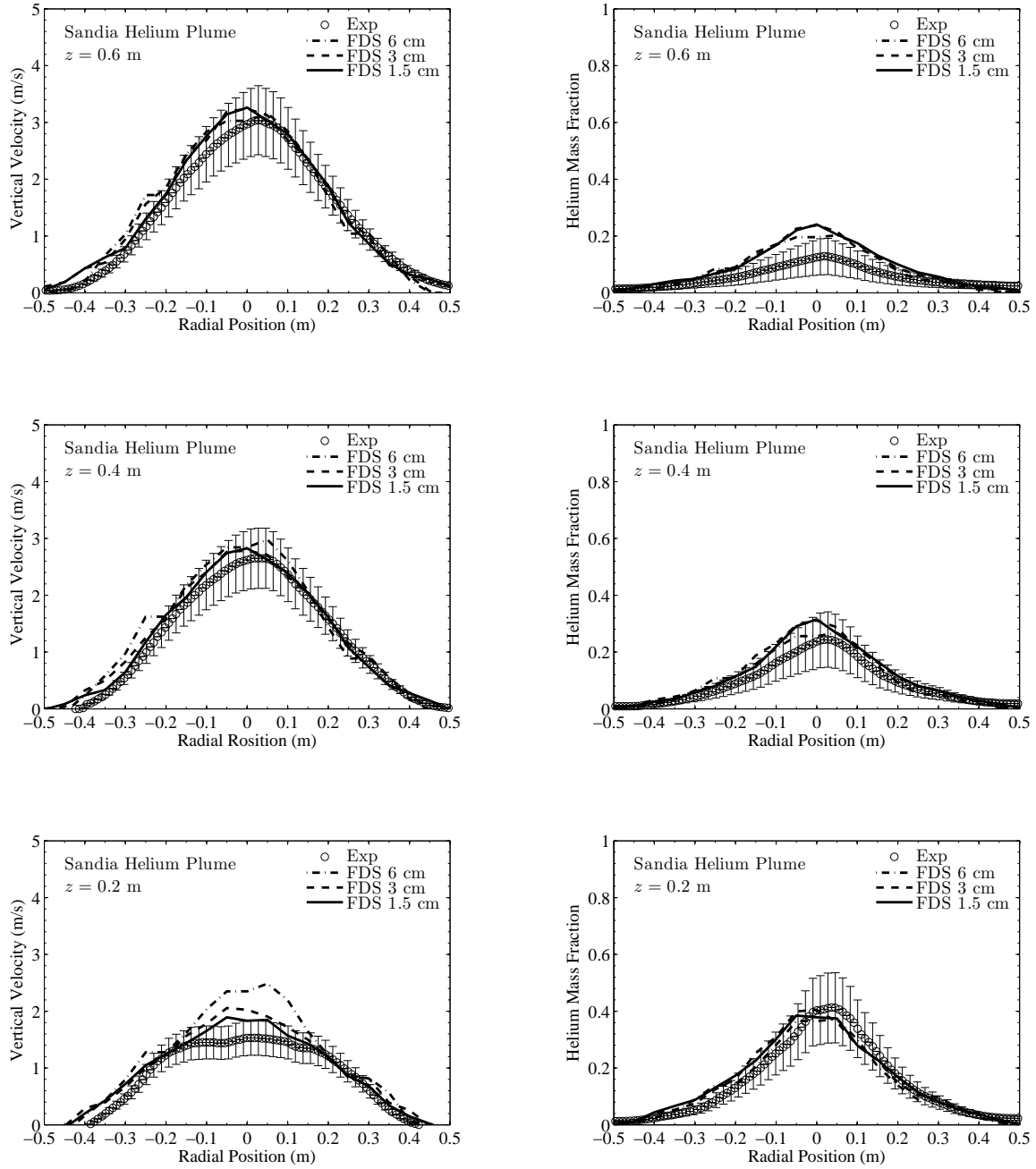


Figure 5: (Left) Mean profiles of vertical velocity. (Right) Mean profiles of helium mass fraction.

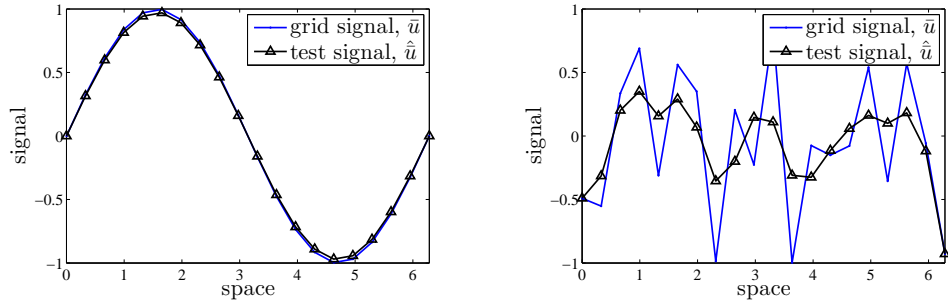


Figure 6: (Left) Resolved signal, MTR is small. (Right) Resolved signal, MTR is close to unity.

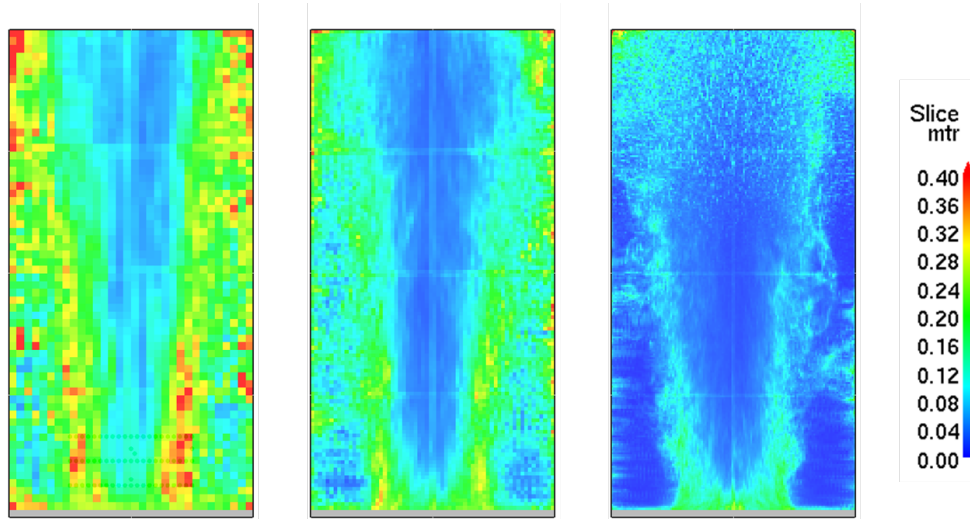


Figure 7: A 10 second time average of MTR (measure of turbulence resolution) for the He plume case at three grid resolutions, from left to right:  $\delta x = \{6, 3, 1.5\}$  cm. The effect of the mesh domain boundaries in the parallel calculation is noticeable because of the way Smokeview draws cell centered data.

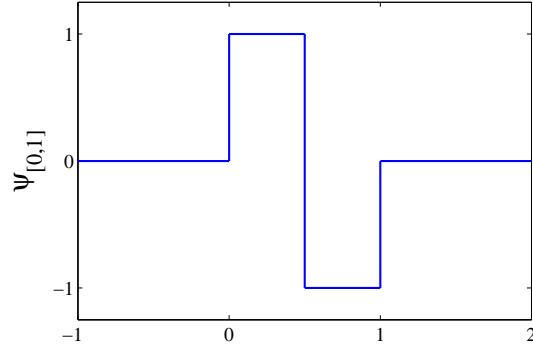


Figure 8: Haar mother wavelet on the interval  $[0,1]$ .

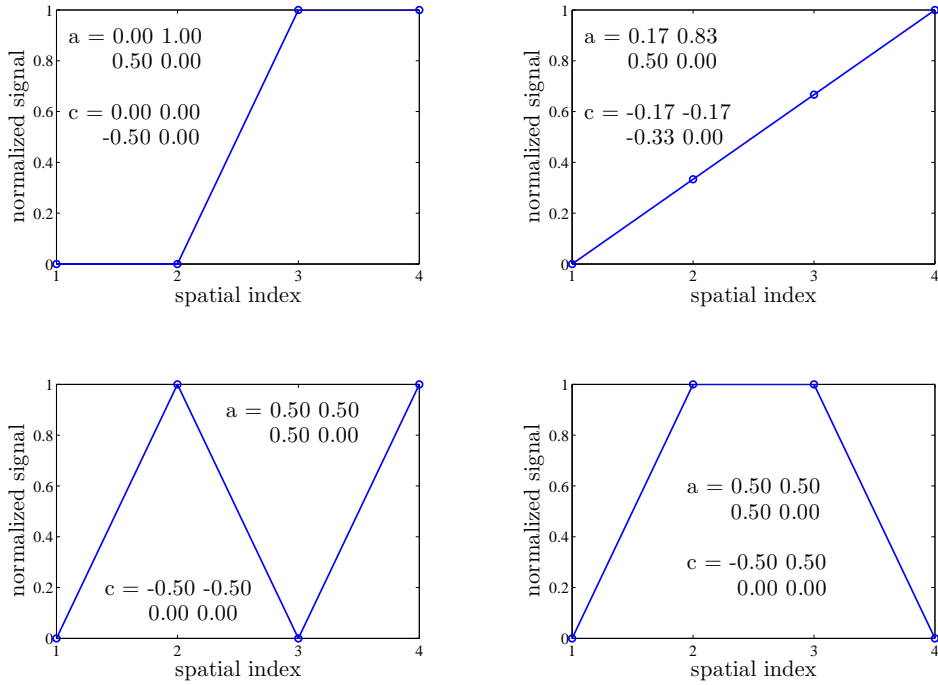


Figure 9: Averages and coefficients for local Haar wavelet transforms on four typical signals.

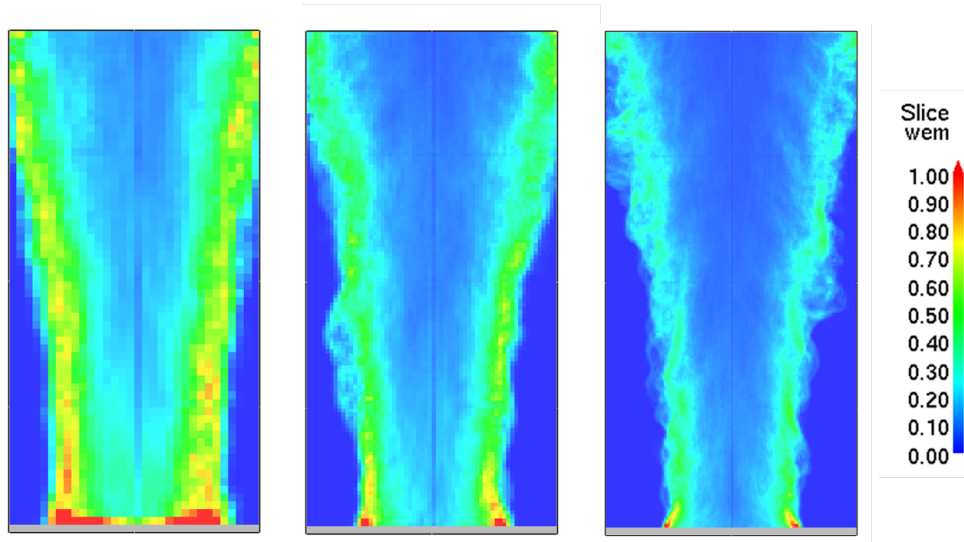


Figure 10: Ten second time averages of wavelet error measure (WEM) at (from left to right) 6, 3, and 1.5 cm resolution.